Climate Dynamics (2023) 60:2219–2234
https://doi.org/10.1007/s00382-022-06421-y

Remote effect of model systematic bias in tropical SST on the cold bias over the Tibetan Plateau

Yuting Wu[1,2] · Xiaoming Hu[2,3,4] · Zhenning Li[5] · Ming Cai[6] · Mengmeng Lu[3,7] · Song Yang[2,3,4]

Received: 22 February 2022 / Accepted: 7 July 2022 / Published online: 11 August 2022

Abstract
Most state-of-the-art climate models substantially underestimate the near-surface air temperature (SAT) over the Tibetan Plateau (TP), especially for the cold season. While previous studies have attributed this cold bias to local factors such as the elevation difference, coarse resolution, and excessive snow cover, this investigation addresses the potential contributions of the systematic bias of tropical sea surface temperature (SST) to the TP cold bias. Experiments with the NCAR Community Atmosphere Model demonstrate that tropical SST bias results in an apparent cold bias over the TP, especially in boreal winter, and explains about 40% of the deviation in multi-model mean SAT over the TP relative to station observations. Forced by the tropical SST bias, heat flux exhibits an anomalous divergence over the plateau, causing a cooling center in the mid- and lower-troposphere over the TP. This atmospheric cooling in turn leads to a reduction of the downward longwave radiative fluxes reaching the surface, less energy supply, and thus a cold bias over the TP.

Keywords Climate models · Tibetan Plateau · Cold bias · Tropical sea surface temperature

1 Introduction

The Tibetan Plateau (TP) exerts a profound impact on atmospheric circulation due to its extraordinary altitude and horizontal extent, and thereby influences the global climate, especially the Asian monsoon climate (Flohn 1957; Yanai et al. 1992; Duan and Wu 2005; Lu et al. 2018, 2019; Wang et al. 2019). Its elevated heating, which is closely associated with the difference between surface skin temperature and surface air temperature (SAT) and related to surface wind speed, is a dominant impacting factor during most of the year (Zhao et al. 2018). As an indicator of the thermal condition of the TP, the SAT is crucial in local air-land interaction and the linkage between the TP and other regions. The TP SAT anomalies could influence the local thermal condition and regulate the climate over downstream regions, plus the phenology over the plateau (Wang et al. 2008; Yu et al. 2010; Xue et al. 2018).

Model simulations have been widely used in studies of the TP SAT due to the lack of observations in the complex geographic environment. However, these simulations often suffer from a cold bias over the TP (Su et al. 2013; You et al. 2016; Jia et al. 2019; Peng et al. 2022). Compared with station observational data, most general climate models

The original online version of this article was revised: "The figures have been placed correctly and affiliation details of author has been updated in the original article."

✉ Xiaoming Hu
huxm6@mail.sysu.edu.cn

✉ Song Yang
yangsong3@mail.sysu.edu.cn

1 Chongqing Research Institute of Big Data, Peking University, Chongqing, China

2 School of Atmospheric Sciences, Sun Yat-sen University, Zhuhai, China

3 Southern Marine Science and Engineering Guangdong Laboratory (Zhuhai), Zhuhai, China

4 Guangdong Province Key Laboratory for Climate Change and Natural Disaster Studies, Sun Yat-sen University, Zhuhai, China

5 Division of Environment and Sustainability, The Hong Kong University of Science and Technology, Hong Kong, China

6 Department of Earth, Ocean, and Atmospheric Science, Florida State University, Tallahassee, FL, USA

7 State Key Laboratory of Severe Weather and Institute of Tibetan Plateau Meteorology, Chinese Academy of Meteorological Sciences, Beijing, China

(GCMs) from the Coupled Model Intercomparison Project Phase 5 (CMIP5) exhibit a substantially cold bias over the plateau, especially during the cold season (Su et al. 2013; Duan et al. 2014; Chen and Frauenfeld 2014). The mean cold bias in CMIP6 models is only slightly reduced in the summertime compared with that in CMIP5 models (Xie & Wang 2021; Lun et al. 2021). Massive effort has been devoted to understanding the sources of the TP cold bias. It was found that the bias of interpolated temperature was in proportion to the increase in local elevation and topographical complexity, and that the improvement of interpolated surface temperature could be achieved via "topographic correction" (Zhao et al. 2008; Hu et al. 2014; Wang et al. 2015). Moreover, the unrealistic local parameterization schemes in models influence surface heat transfer and resistance, which is partly responsible for the TP SAT bias (Yang et al. 2007; Zhuo et al. 2016). Lee et al. (2019) also reported that the lack of ice radiative effect (i.e. the miss of emission from falling snow) in most CMIP5 models, causing more solar radiation to penetrate through the optically thin atmosphere and less downward longwave (LW) radiation, could also explain a portion of the model biases of surface radiative fluxes and surface temperature over the TP. Several studies focused on the land processes in model simulations, especially the snow processes, further found that overestimation of TP snow could lead to larger solar energy reflection and then a colder surface and that the simulated cold bias would be improved with more realistic albedo over the TP (Rangwala et al. 2010; Ghatak et al. 2014; You et al. 2016; Meng et al. 2018).

Apparently, the aforementioned studies have been mainly focused on the local processes that may induce cold bias in models. However, the TP SAT is simultaneously regulated by tropical sea surface temperature (SST). The spring SST and air-sea coupling of the Indian Ocean significantly affect the TP heat source in summer, and the Indian Ocean SST and TP SAT exhibit a possibly teleconnected mode (Zhang et al. 2006; Ji et al. 2018; Zhao et al. 2018; He et al. 2019; Wang et al. 2019). Besides, El Niño is closely associated with an increase in wintertime snowfall over the plateau, causing a colder TP (Shaman and Tziperman 2005); Wang and Xu 2018) . The remote SST in the warm pool could also govern TP warming by modulating the coherent variations of tropical easterly jet stream and subtropical westerly jet stream (Wang et al. 2012). Ma et al. (2017) suggested that the tropical and extratropical oceanic internal variability exerted a relatively uniform warming effect on the whole TP during 1980–2012.

While SST especially the tropical SST shows a profound influence on the TP SAT as discussed above, the SST itself displays a remarkable systematic bias in the state-of-the-art models. SST errors are comparable or even larger than the observed interannual variability and the projected change of SST in the 21st century (Li and Xie 2012). The equatorial cold tongue penetrates too far westward in the Pacific with a double intertropical convergence zone (Mechoso et al. 1995; Li and Xie 2014; Zhou et al. 2020), and there exist warm SST biases over the southeastern Pacific off South America (Xie et al. 2007; de Szoeke et al. 2010). Also, the warm SST bias in the southeastern tropical Atlantic is a common problem in many previous and current climate models (Xu et al. 2014; Zhang et al. 2014; Exarchou et al. 2018; Kurian et al. 2021), and coupled atmosphere-ocean GCMs show substantial difficulties in correctly simulating the sign of the near-equatorial zonal gradient of the Atlantic Ocean SST (Davey. et al. 2002; DeWitt 2005; Song et al. 2012).

Given that tropical SST influences the TP SAT extensively and that climate models often suffer from large biases especially over the tropical Pacific and Atlantic oceans, the unrealistic climatological SST in model simulations may also contribute to the TP SAT bias. The current study is aimed to explore the possible role of tropical SST biases in the modeled TP cold biases. In Sect. 2, datasets, model design, and analysis methods are introduced. Section 3 describes the TP cold bias and the tropical SST bias in climate models. Section 4 presents the influence of tropical SST bias forcing on the TP SAT bias and the responsible mechanisms. Summary and discussion are presented in Sect. 5.

2 Data, model design and method

2.1 Data

The Extended Reconstructed SST version 5 (ERSSTv5; Huang et al. 2017) dataset from the National Oceanic and Atmospheric Administration (NOAA) and the SAT dataset from the National Meteorological Information Center (China Meteorological Administration, http://data.cma.cn/data/cdcdetail/dataCode/SURF_CLI_CHN_TEM_MON_GRID_0.5.html) are used as the observed references to calculate models' systematic biases. The monthly gridded SAT data during 1961–2018 with a high spatial resolution of 0.5° × 0.5° are interpolated from the observation records of more than 2400 Chinese meteorological stations. The SST segment from the ERSSTv5 dataset is from 1950 to 1999 on 2° × 2° resolution grids. The domain of the TP is limited to the area higher than 1500 m over 25°–40°N/75°–105°E.

Model biases are defined as the deviations of model simulations in historical experiments from the observed monthly SAT and surface skin temperature. Note that the values of surface skin temperature over the oceans are the same as the SST in climate models. The systematic bias is the mean of model deviations obtained from 28 CMIP5 models and

20 CMIP6 models. Tables S1 and S2 in the supplemental materials provide a summary of the details of all model simulations. To facilitate a comparison with observations, all the simulated SAT and SST data by the GCMs are interpolated to 0.5˚ × 0.5˚ and 2˚ × 2˚ grids, respectively. Since previous studies have demonstrated a robust annual cycle of the strength of TP cold bias (Su et al. 2013; Jia et al. 2019), all model biases analyzed in this study are measured by monthly mean values.

2.2 Model and experiment design

The model used in this study is the Community Atmosphere Model version 4 (CAM4), the atmospheric component of the Community Earth System Model version 1.2.2 (CESM 1.2.2) from the National Center for Atmospheric Research (NCAR, Neale et al. 2013), with a horizontal resolution of 1.25˚ longitude by 0.9˚ latitude and 26 vertical levels. The CESM as a fully-coupled global climate model can provide state-of-the-art simulations of the climate states and be used for a broad class of scientific research (Hurrell et al. 2013).

This study is mainly based on six model experiments, whose design is briefly described in Table 1. The simulations are implemented by F_AMIP component setting, in which both the atmosphere model and land surface model are active. The control experiment, referred to as CTRL, is forced by the observed monthly-mean global SST from 1979 to 2005. The surface boundary forcing dataset for uncoupled simulations with CAM4 is a merged product based on the monthly-mean Hadley Center Sea Ice and Sea Surface Temperature dataset (HadISST) and the NOAA Optimum Interpolation Sea Surface Temperature dataset (OISST). The details about the default optional product have been described in Hurrell et al. 2008). It should be noted that the TP SAT bias exists in the CTRL experiment which is forced by observed SST. The TP bias can be attributed to not only remote factors (e.g. tropical SST bias) but also local factors such as surface heat fluxes, snow cover, and so on. Therefore, the TP SAT bias can still exist even though the model is forced by observed SST. We can remove this inherent bias by using the difference between the perturbation and control simulations to represent the contribution of tropical SST bias. The second to fifth sensitivity experiments are similar to the CTRL, except that the annual cycle of tropical (30˚S-30˚N) SST bias is imposed on the observed monthly-mean global SSTs over all the three basins (referred to as SEN-ALL), the Pacific Ocean basin only (referred to as SEN-PAC), the Atlantic Ocean only (referred to as SEN-ATL), and the Indian Ocean only (referred to as SEN-IND), respectively. It is noted that the tropical SST bias is given by the climatological monthly SST difference between the CMIP5 multi-model ensemble (MME) and the ERSSTv5 during 1950–1999. The last sensitivity experiment (referred to as SEN-ALL6) is similar to SEN-ALL, except that the tropical SST bias is replaced by the difference between the CMIP6 MME and the ERSSTv5. All experiments involve model runs for 27 years and the results from the last 25 years are analyzed.

Table 1 Description of model design and experiments

Name	Abbr.	Description
Ctrl run	**CTRL**	Observed SST forcing
All-basin tropical SST bias run	**SEN-ALL**	Observed SST forcing + CMIP5 tropical (30°S-30°N) SST bias with annual cycle only
Pacific Ocean basin tropical SST bias run	**SEN-PAC**	Observed SST forcing + CMIP5 Pacific Ocean basin tropical (30°S-30°N) SST bias with annual cycle only
Atlantic Ocean basin tropical SST bias run	**SEN-ALT**	Observed SST forcing + CMIP5 Atlantic Ocean basin tropical (30°S-30°N) SST bias with annual cycle only
Indian Ocean basin tropical SST bias run	**SEN-IND**	Observed SST forcing + CMIP5 Indian Ocean basin tropical (30°S-30°N) SST bias with annual cycle only
CMIP6 all-basin tropical SST bias run	**SEN-ALL6**	Observed SST forcing + CMIP6 tropical (30°S-30°N) SST bias with annual cycle only

2.3 Method

2.3.1 Downward LW radiation decomposition

We apply the radiative transfer model by Fu and Liou (1992, 1993) to decompose the total downward LW radiative surface energy flux perturbations ($\Delta R_s\downarrow$) between CTRL and SEN-ALL into the sum of partial downward LW surface energy flux perturbations due to the changes in CO_2 ($\Delta R_s^{CO2}\downarrow$), ozone ($\Delta R_s^{O3}\downarrow$), cloud ($\Delta R_s^{Cloud}\downarrow$), water vapor ($\Delta R_s^{WV}\downarrow$), and air temperature ($\Delta R_s^{TA}\downarrow$). The decomposition can be expressed mathematically as:

$$\Delta R_s\downarrow \approx \Delta R_s^{CO2}\downarrow + \Delta R_s^{O3}\downarrow + \Delta R_s^{Cloud}\downarrow + \Delta R_s^{WV}\downarrow + \Delta R_s^{TA}\downarrow \quad (1)$$

where the subscript s denotes the near-surface layer and R represents LW radiation. In fact, each term in the right-hand side of Eq. (1) is calculated as the difference between two runs of the radiative transfer model: one with the fields of CO_2, ozone, clouds, water vapor, and air temperature derived from CTRL and the other with identical inputs except the fields denoted by the superscripts, which are taken from experiment SEN-ALL. For the left-hand side $\Delta R_s\downarrow$, the inputs of the first radiative transfer model calculation are all taken from CTRL and the fields for the second calculation are all from SEN-ALL. Considering the same external

forcing fields of CO_2 and ozone in CTRL and SEN-ALL, $\Delta R_s^{CO2}\downarrow$ and $\Delta R_s^{O3}\downarrow$ are expected to be zero. Therefore, we do not present the results of $\Delta R_s^{CO2}\downarrow$ and $\Delta R_s^{O3}\downarrow$ in Sect. 4.3.

Furthermore, we apply the coupled feedback response analysis method (CFRAM) by Cai and Lu (2009) and Lu and Cai (2009) to decompose the total air temperature changes into partial air temperature changes due to individual processes including water vapor and others. This approach allows us to further evaluate the downward LW radiative flux (DLWRF) anomalies at the surface associated with the partial air temperature anomalies due to individual processes. To be specific, we use

$$\Delta T^X \approx \left(\frac{\partial R}{\partial T}\right)^{-1} \Delta Q^X \tag{2}$$

to evaluate the vertical profile of partial temperature anomalies (ΔT^X in units of K) from the vertical profile of partial radiative or non-radiative heating anomalies due to a specific process "X" (ΔQ^X in units of W/m^2). In Eq. (2), $(\partial R/\partial T)$ is the Planck feedback matrix whose *j*th column corresponds to the vertical profile of the radiative energy perturbation due to 1-K warming at the *j*th layer. There are five radiative processes of "X", namely, CO_2 concentration $\left(\Delta Q^{CO2}\right)$, ozone $\left(\Delta Q^{O3}\right)$, water vapor $\left(\Delta Q^{WV}\right)$, cloud $\left(\Delta Q^{Cloud}\right)$, and surface albedo (ΔQ^{α}). All the five terms can be obtained from the same calculation as for the right-side terms in Eq. (1). Besides, non-radiative processes $\left(\Delta Q^{NR}\right)$ such as surface turbulent sensible and latent heat fluxes, atmospheric large-scale advective and convective processes, and heat storage terms in the surface and atmospheric layers can also induce energy flux convergence anomalies. Estimation of the vertical profile of total non-radiative heating perturbations is based on the energy balance between radiative and non-radiative processes. That is,

$$\Delta Q^{NR} = -\Delta Q^{R} \tag{3}$$

where ΔQ^R corresponds to the vertical profile of radiative energy flux convergence due to the changes in all the radiative processes. ΔQ^R can be derived from the same-way calculation of the left-side term in Eq. (1). We further divide the ΔQ^{NR} into the surface part ΔQ^{NRS} and the atmospheric part ΔQ^{NRA}, where ΔQ^{NRS} represents the surface turbulent heat flux process and heat storage term, with its atmospheric component set to zero, and ΔQ^{NRA} represents the atmospheric large-scale advective and convective processes, with its surface component set to zero.

Finally, according to Eq. (2), we obtain the total seven partial temperature anomaly fields induced by CO_2 concentration $\left(\Delta T^{CO2}\right)$, ozone $\left(\Delta T^{O3}\right)$, water vapor $\left(\Delta T^{WV}\right)$, cloud $\left(\Delta T^{Cloud}\right)$, surface albedo (ΔT^{α}), surface dynamic processes $\left(\Delta T^{NRS}\right)$, and atmospheric dynamic processes $\left(\Delta T^{NRA}\right)$. Then, the DLWRF anomalies at the surface associated with the partial air temperature anomalies related to ΔT^X can be obtained according to (after the linearization approximation),

$$\Delta R_s^{TA\_X}\downarrow = \sum_{j=1}^{J}\left(-\frac{\partial R_s}{\partial T_j}\right)\Delta T_j^X \tag{4}$$

where $\left(-\frac{\partial R_s}{\partial T_j}\right)$ corresponds to the DLWRF perturbations at the surface layer due to a 1-K warming at the *j*th layer (for model outputs, J = 26). By substituting the atmospheric component of all seven ΔT^X terms obtained by Eq. (2) into Eq. (4), we have seven $\Delta R_s^{TA\_X}\downarrow$ terms, and the sum of these $\Delta R_s^{TA\_X}\downarrow$ terms is close to $\Delta R_s^{TA}\downarrow$ in Eq. (1). Specifically, $\Delta R_s^{TA\_CO2}\downarrow$ and $\Delta R_s^{TA\_O3}\downarrow$ are expected to be zero due to the same forcing of CTRL and SEN-ALL, while $\Delta R_s^{NRS}\downarrow$ and $\Delta R_s^{\alpha}\downarrow$ are smaller than the other three remaining $\Delta R_s^{TA\_X}\downarrow$ terms because these two terms are cancelled with each other, and, as discussed in Sejas and Cai (2016) and Hu et al. (2017), they represent the effect of air temperature response to the energy flux perturbations at the surface whereas other three $\Delta R_s^{TA\_X}\downarrow$ terms include the effect of air temperature response to the energy flux perturbations both at the surface and in the atmosphere. In summary, we obtain,

$$\Delta R_s^{TA}\downarrow \approx \Delta R_s^{TA\_Cloud}\downarrow + \Delta R_s^{TA\_WV}\downarrow + \Delta R_s^{TA\_NRA}\downarrow \tag{5}$$

to further decompose the DLWRF anomalies induced by air temperatures into the partial DLWRF anomalies due to cloud, water vapor, and atmospheric dynamic processes. .

2.3.2 Offline error correction

According to Eq. (1), offline errors come from the difference between $\Delta R_s\downarrow$ and the sum of $\Delta R_s^X\downarrow$. They are attributed to (i) using the climatological mean fields as inputs of the radiative transfer model in our offline calculations instead of the climatological mean of taking the radiative heating rates calculated by the instantaneous fields, especially for the cloud fields (Kang et al. 2020), (ii) adopting different radiative transfer models, and (iii) excluding the changes in other processes such as aerosols.

Following Hu et al. (2017), we identify the dominant terms that are responsible for $\Delta R_s^{err}\downarrow$ by comparing the spatial distribution of each term $\left(\Delta R_s^X\downarrow\right)$ in the right-hand side of Eq. (1) with error $(\Delta R_s^{err}\downarrow)$. We evaluate the pattern correlation (r^X) between each individual process $\Delta R_s^X\downarrow$ and error $\Delta R_s^{err}\downarrow$ over region *A*, namely,

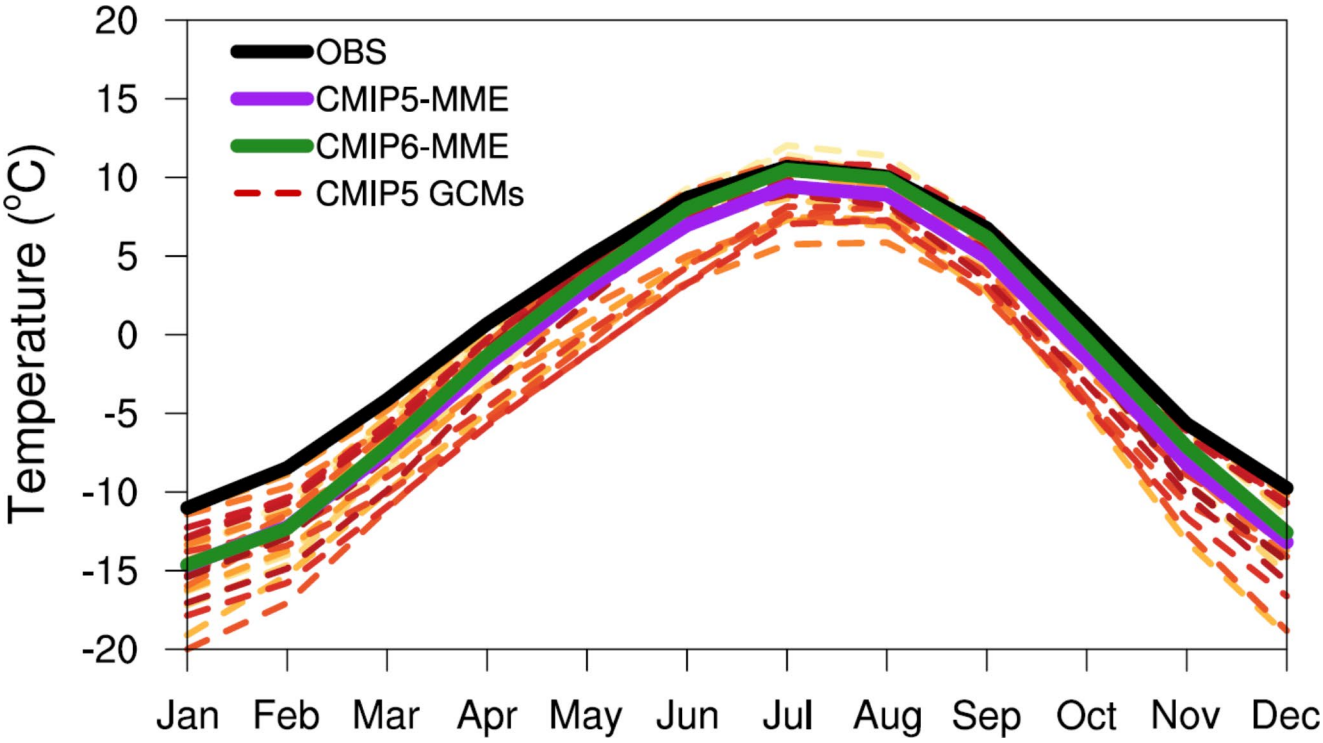

Fig. 1 Climatological monthly-mean surface air temperatures (units: ˚C) for 1961–2005 over the TP. Black solid line depicts the observation, the dashed lines and purple solid line denote the values of 28 CMIP5 models and the multi-model ensemble mean, and the green solid line denotes the CMIP6 multi-model ensemble mean

$$r^X = \frac{A^{-1}\int_A a^2 \Delta R_s^X \Delta R_s^{err} cos\phi d\lambda d\phi}{\sqrt{A^{-1}\int_A a^2 (\Delta R_s^{err})^2 cos\phi d\lambda d\phi}} \quad (6)$$

where ϕ and λ are latitude and longitude, respectively. A indicates the TP region in this study, and a is the mean radius of the earth. It is found that r^{Cloud}, the spatial pattern correlation between $\Delta R_s^{err}\downarrow$ and $\Delta R_s^{Cloud}\downarrow$ is the largest among the three processes, which is up to -0.5. The strong negative correlations suggest that the input of time-mean cloud fields tends to overestimate the DLWRF of the cloud feedback.

To address the above issue about overestimation, we correct the DLWRF perturbations of the offline error fields by removing the counterparts of the partial DLWRF due to the changes in clouds, namely,

$$\begin{cases} correction\_\Delta R_s^{Cloud} = \Delta R_s^{Cloud} + r^{Cloud} * \Delta R_s^{Cloud} \\ correction\_\Delta R_s^{err} = \Delta R_s^{err} - r^{Cloud} * \Delta R_s^{Cloud} \end{cases} \quad (7)$$

The corrected DLWRF perturbations due to the changes in cloud are shown in this paper while the uncorrected results are omitted.. The same method is used in the further decomposition of the downward LW flux perturbations due to the changes in atmospheric temperatures as given by Eq. (5), where the offline error mainly comes from the atmospheric dynamic process instead of the cloud field.

3 TP cold bias and tropical SST bias

Figure 1 shows the climatological monthly mean SAT over the TP in observation, CMIP5 models, and CMIP6 models. Both the CMIP5 and CMIP6 MMEs can reproduce the annual cycle of the TP SAT, but with a cold bias, especially in the cold season. Compared with the observation (black solid line), almost all CMIP5 models (dashed lines) significantly underestimate the TP SAT throughout the year, with the annual mean cold biases ranging from − 5.54 K to 0.04 K. The CMIP5 MME (purple solid line) presents a larger cold bias (-3.62 K) in boreal winter and a smaller one (-1.38 K) in boreal summer. Compared with CMIP5, the CMIP6 MME (green solid line) shows a progress in boreal summer, with a bias of about − 0.33 K, but a comparable cold bias in boreal winter, with a magnitude of -3.43 K.

Figure 2a shows the correlation between the annual-mean TP SAT and global SST in observations. The TP SAT is closely related to tropical SST, especially that in the tropical Pacific and Atlantic oceans. The multi-model mean of correlation coefficients derived from the individual CMIP5 models displays a remarkably high correlation coefficient

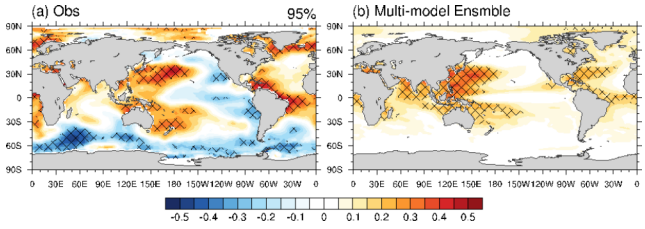

Fig. 2 Correlations between the annual-mean TP surface air temperature and the annual-mean global SST of **a** observations and **b** CMIP5 multi-model ensemble mean. Note that (b) is given by the multi-model mean of each model's correlation coefficient. The cross-slashed areas in **a** indicate the shaded values exceeding the 95% confidence level of statistical significance, and the cross-slashed areas in **b** indicate that the shaded values exceed one standard deviation of the model correlation coefficient

between the SAT and the SST (Fig. 2b), and the large values in tropical oceans indicate that the models reach a consensus on the significant correlation. The difference between Fig. 2a and b mainly rises from two aspects: the lack of observational data over the Southern Ocean produces potentially unrealistic correlation (Sumner et al. 2003; Rapizo et al. 2015) and climate models vary widely in their simulations of the Southern Ocean and its climate impact (Russell et al. 2018).

Figure 3 displays the spatial pattern of monthly-mean and annual-mean tropical SST biases in CMIP5 MME relative to observations. The biases exhibit a small annual cycle, with a large region of cold bias and a smaller region of warm bias. The main cold bias appears in the tropical Pacific and Atlantic oceans, while the main warm bias emerges from the east coast of the mainland like Peru and western Africa. The tropical Indian Ocean shows a relatively large cold bias in the cold season and a smaller bias in the warm season. The tropical SST bias of the CMIP6 MME illustrates similar patterns with the CMIP5 MME, but with a relatively smaller magnitude (Fig. S1 in the supplemental materials).

Given the close relationship between the TP SAT and the tropical SST, one may naturally ask whether the systematic cold bias over the TP presented in Fig. 1 can be partially explained by the tropical SST bias shown in Fig. 3. To gain an insight onto this question, we construct two indices: E_{SST} and E_{TP}, with the former for the severity of SST bias and the latter for the severity of TP SAT bias of individual models. Specifically, the index E_{TP} is defined as the areal-mean and annual-mean TP SAT bias of the individual CMIP5 models, whereas the index E_{SST} is the projection coefficients of tropical SST bias from individual models onto the MME SST bias. That is

$$E_{SST}(j) = \frac{A^{-1}\int_A a^2(SST_j - \mathrm{SST}_{OBS})(SST_{MME} - \mathrm{SST}_{OBS})\cos\phi d\lambda d\phi}{\sqrt{A^{-1}\int_A a^2(SST_{MME} - \mathrm{SST}_{OBS})^2\cos\phi d\lambda d\phi}} \quad (8)$$

where $(SST_{MME} - SST_{OBS})$ is the climatological annual-mean SST bias derived from the CMIP5 MME (i.e. Figure 3m), SST_j is the climatological annual mean SST of the CMIP5 model *j*, and SST_{OBS} corresponds to the climatological annual mean SST in observations. Besides, other parameters have the same meanings as those in Eq. 6, except that *A* represents the tropical ocean domain (30°S–30°N).

Figure 4 is the scatter plot of the two indices. The index E_{SST} ranges from 0.61 to 1.22 K and E_{TP} ranges from − 5.54 K to 0.04 K. The non-negative values of E_{SST} indicate that all CMIP5 models have similar spatial patterns of SST bias with the same polarity as the MME SST bias shown in Fig. 3m. By definition, the models with smaller (larger) values of index E_{SST} would perform better (worse) in reproducing the observed tropical SST or suffer from a smaller (greater) SST bias. The negative correlation (about − 0.4) between E_{TP} and E_{SST} of individual models indicates that smaller E_{SST} corresponds to a larger E_{TP} (i.e. a smaller cold bias), which indeed confirms that the models with a better (worse) ability of reproducing tropical SST would perform better (worse) in reproducing the SAT over the TP. Such a negative correlation is consistent with the observed feature shown in Fig. 2, namely cold SST bias over the tropical Pacific (which corresponds to positive projection onto Fig. 3m) would partially account for the cold SAT anomalies over the TP. Moreover, the non-perfect correlation between these two indices may be due to that the cold TP response to the tropical SST bias is nonlinear and that other factors (such as local effects) besides tropical SST bias also contribute to the cold TP bias.

To further substantiate the above statistical evidence that the systematic cold bias over the TP could be partially originated from the tropical SST bias, we perform a series of model experiments forced by tropical SST biases using the NCAR CAM4 model. The modeling experiments would help shed light on the underlying mechanisms for the cold response over the TP to tropical SST biases.

4 Results from model experiments

4.1 Change in TP SAT forced by tropical SST bias

Figure 5a - l show the spatial distributions of SAT difference between experiments SEN-ALL and CTRL from January to December. Under the CMIP5 MME tropical SST bias forcing, the TP SAT experiences an obvious cooling with strong signals in the cold season and relatively weaker signals in the warm season, which is similar to the feature shown in Fig. 1. The TP SAT anomaly forced by tropical SST bias can also reproduce the spatial distribution of MME cold bias in CMIP5/6 to some degree, which is larger over

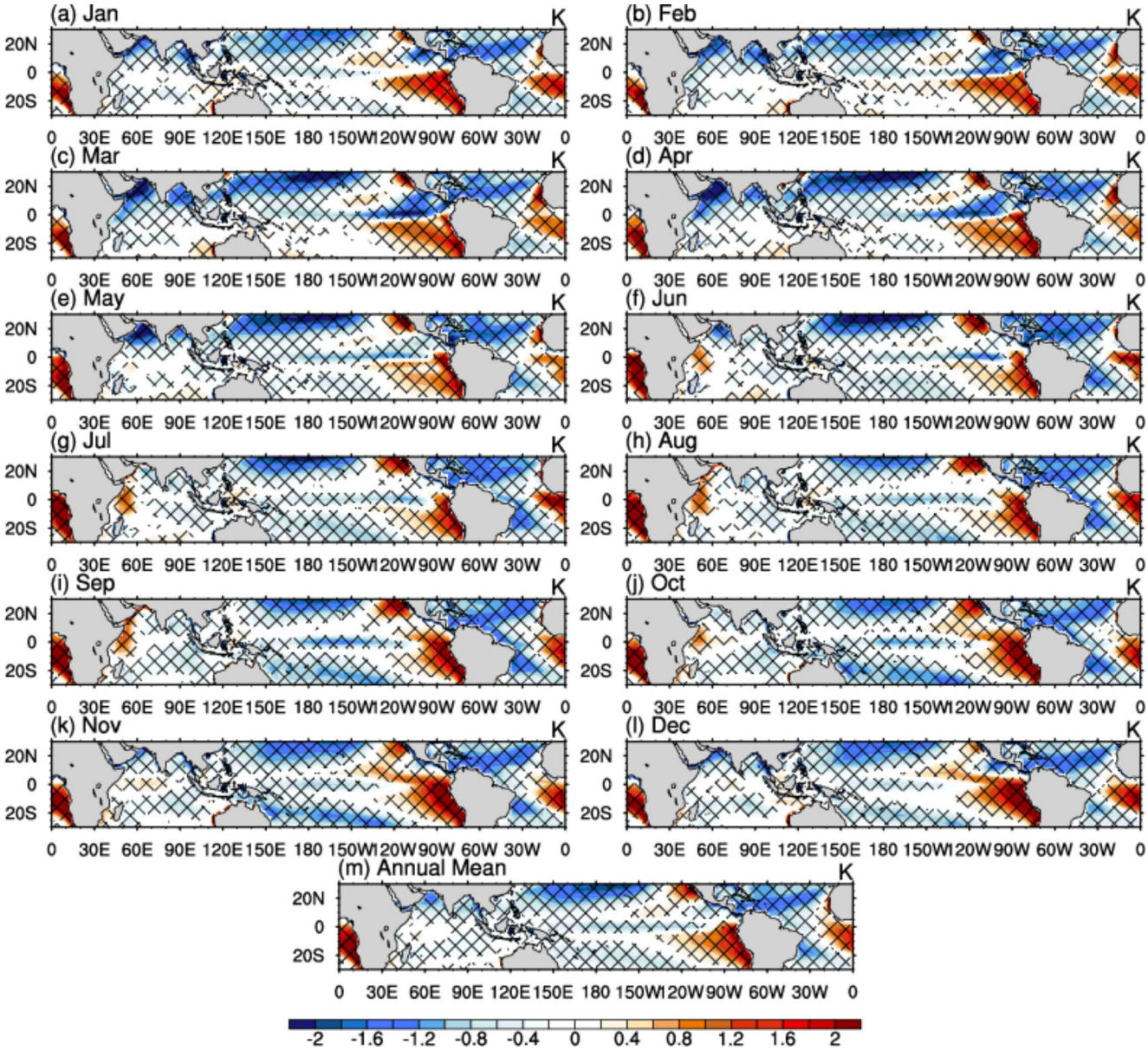

Fig. 3 Spatial patterns of CMIP5 multi-model ensemble mean tropical SST bias (units: K) with respect to observation from **a** January to **l** December, and **m** the annual mean for 1950–1999. The cross-slashed areas indicate the shaded values exceeding the 95% confidence level of statistical significance

the western TP and smaller over the central and eastern TP. Figure 5m presents the area-averaged change in TP SAT in different tropical SST bias runs with respect to the CTRL, which displays that the tropical SST bias forcing by both CMIP5 MME and CMIP6 MME would lead to a cooler surface over the TP with an analogous annual cycle. In boreal winter, SEN-ALL (SEN-ALL6) shows a cold bias of about 1.49 K (1.31 K), which explains about 41% (38%) of the total winter cold bias in Fig. 1. Moreover, under the individual forcing of the tropical Pacific, Atlantic, and Indian Ocean SST biases, the TP exhibits an anomalous surface cooling of about − 0.65 K, -0.64 K, and − 0.31 K in winter and − 0.25 K, -0.01 K, and − 0.24 K in summer, respectively. Apparently, the tropical Pacific shows the largest contribution to the total cold bias forced by the tropical SST biases. Nevertheless, it should be noted that the contribution of each basin is not linearly addable due to the complex interaction among the three ocean basins.

Thus, the systematic tropical SST bias forcing of each ocean basin, especially the forcing of tropical Pacific bias, could explain a portion of the systematic cold bias over the TP. Here, we focus on the collective contributions of SST bias in all the three tropical basins to the TP cold bias in boreal winter, and the following analysis will be based on

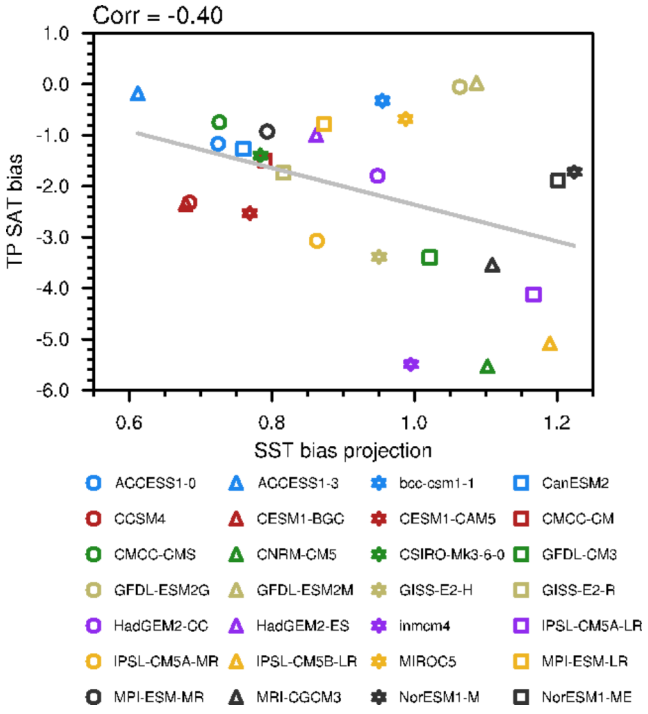

Fig. 4 Scatter plot of tropical SST bias projection (K) and TP SAT bias (K) indices derived from CMIP5 historical climate simulations. The grey line is least-squares regression fits to data points. The value in the upper left indicates the corresponding correlation coefficient

the outputs from CTRL and SEN-ALL for the December-January-February (DJF) means.

4.2 Surface energy budget analysis of winter TP cooling

The sources of winter surface cooling over the TP can be revealed via a surface energy budget analysis. According to the Stefan-Boltzmann law, the upward LW radiation is directly proportional to surface temperature. The surface cooling over the TP is equivalent to the decrease in upward LW radiation. Based on the surface energy budget equation, this decrease in upward LW radiation is coupled with the changes in downward LW radiation, upward and downward shortwave (SW) radiation, latent heat flux (LH), sensible heat flux (SH), and ground heat flux (G0) at the surface. That is,

$$\Delta R_s\uparrow = \Delta R_s\downarrow + \Delta S_s\downarrow - \Delta S_s\uparrow - \Delta SH\uparrow - \Delta LH\uparrow - \Delta G_0\uparrow \quad (9)$$

where the subscript $_s$ denotes the surface layer, and R and S represent LW and SW radiations, respectively. Figure 6 illustrates the spatial distributions of the changes in winter surface energy fluxes between SEN-ALL and CTRL. The upward LW radiation (Fig. 6a) is much smaller in SEN-ALL than in CTRL, which is consistent with the cooler TP in SEN-ALL. The decreased upward LW radiation is balanced by (1) the obviously decreased downward LW radiation (Fig. 6b), (2) the increased downward and upward SW radiations (Fig. 6d and e), and (3) the small changes in SH, LH, and G0 (Fig. 6g, h, and i). The changes in surface SH, surface LH, and G0 are relatively small compared with those in surface radiative heat fluxes and thus are neglectable. Also, the sum of these three terms seems positive, indicating that the net effect of the biases in SH, LH, and G0 would lead to more energy going to the surface layer (or less energy leaving the surface layer). Moreover, the total effect of LW radiation change exhibits a decreased net LW radiation (Fig. 6c, positive value indicating downward) over the nearly entire TP, suggesting that the decreased downward LW is dominant so that the surface loses energy via LW radiation. However, the total effect of SW radiation change, i.e. the net SW radiation (Fig. 6f, positive value indicating downward), shows a small increase over the central and western TP and a small decrease over the eastern TP, which indicates more solar radiation supply. These results of surface energy budget over the TP suggest that the plateau gains more energy via SW radiation and surface non-radiative processes but loses more energy via LW radiation. The decrease in surface downward LW radiation from the atmosphere is the dominant contributor to the decreased SAT over the TP.

Then, which factors are responsible for the decreased downward LW radiation under the forcing of tropical SST bias? To answer this question, we adopt the Fu and Liou (1992, 1993) radiative transfer model (see Sect. 2) to decompose the reduction of DLWRF.

4.3 Decomposition of winter downward LW radiative fluxes

The decreased surface DLWRF in Fig. 6b has been decomposed into the LW perturbations due to the changes in cloud (Fig. 7a), water vapor (Fig. 7b), and air temperature (Fig. 7c). The sum of the partial surface DLWRF (Fig. 7a, b, and c) is shown as the shading in Fig. 7d, which is close to the model output (the contour of Fig. 7d). The error term, namely the difference between the shading and the contour of Fig. 7d, is small, indicating that the decomposition is reasonable and valid (figure not shown). It is also found that the change in clouds mainly leads to a decreased DLWRF over the central TP, while the change in water vapor causes a generally uniformly-reduced DLWRF over the entire TP. Moreover, the change in air temperature is the largest contributor to the total downward LW perturbation, causing larger DLWRF over the western TP and smaller DLWRF over the eastern TP. The decreased DLWRF due to the change in air temperature is mainly caused by the cold atmosphere over the TP (Fig. S2 in the supplemental materials).

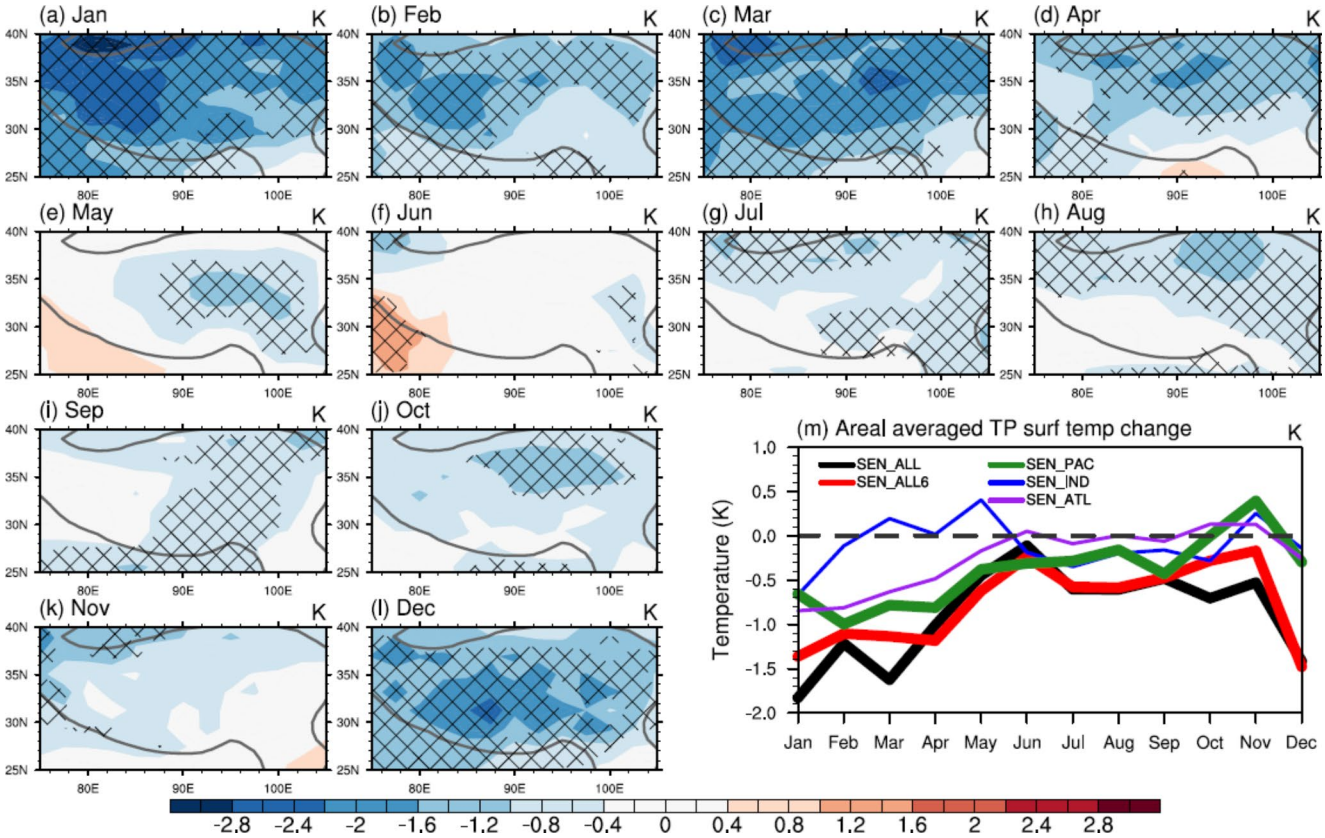

Fig. 5 Spatial patterns of difference in surface air temperature (units: K) between CTRL and SEN-ALL from **a** January to **l** December. The cross-slashed areas indicate the temperature change that exceeds the 95% confidence level of statistical significance. The grey solid lines denote the topographic height of 1500 m. **m** Areal averaged change in TP surface air temperature (units: K) in different tropical SST bias runs with respect to CTRL

To reveal the origins of the anomalous atmospheric cooling over the TP, we further decompose the surface DLWRF perturbations induced by air temperature anomalies into three terms, i.e. partial air temperature anomalies associated with the changes in cloud, water vapor, and large-scale atmospheric heat transport. As shown in Fig. 8a, the reduction of DLWRF due to the cloud-induced air temperature change is mainly located over the southeastern TP and the western TP, and the reduction due to the water vapor induced change in air temperature is approximately uniform over the TP with a relatively larger magnitude over the western TP (Fig. 8b). Moreover, the reduction due to air temperature anomalies is dominated by the non-radiative heating contribution from the atmospheric advective and convective processes over the central TP (Fig. 8c). The shading in Fig. 8d, which is the sum of Fig. 8a, b, and c, shows the anomalously decreased DLWRF over the western and southeastern TP. The originally-decomposed DLWRF perturbations induced by anomalous atmospheric temperature are shown in Fig. 8d (contour), with a decreased magnitude of DLWRF reduction along the western TP to the eastern TP. The difference between the shading and the contour in Fig. 8d presents that negative errors are mainly limited to the central TP, with positive errors in the southeastern TP (values not shown), suggesting an underestimation of decomposition over the central TP and an overestimation over the southeastern TP. Since the decreased DLWRF is mainly affected by atmospheric dynamic processes, it is worth exploring the possible link between the change in atmospheric circulation and the decreased DLWRF induced by anomalous atmospheric cooling.

4.4 Changes in winter heat flux convergence and large-scale atmospheric circulation

As discussed above, atmospheric dynamic processes play an important role in the anomalous atmospheric cooling that leads to a decreased DLWRF over the TP. Heat flux divergence is a main atmospheric dynamic process that may be responsible for the change in air temperature. Figure 9a, which is the same as Fig. 8c but with a different color bar for a better comparison in the following analysis, shows the DLWRF perturbations due to the anomalous atmospheric temperature induced by atmospheric dynamic processes,

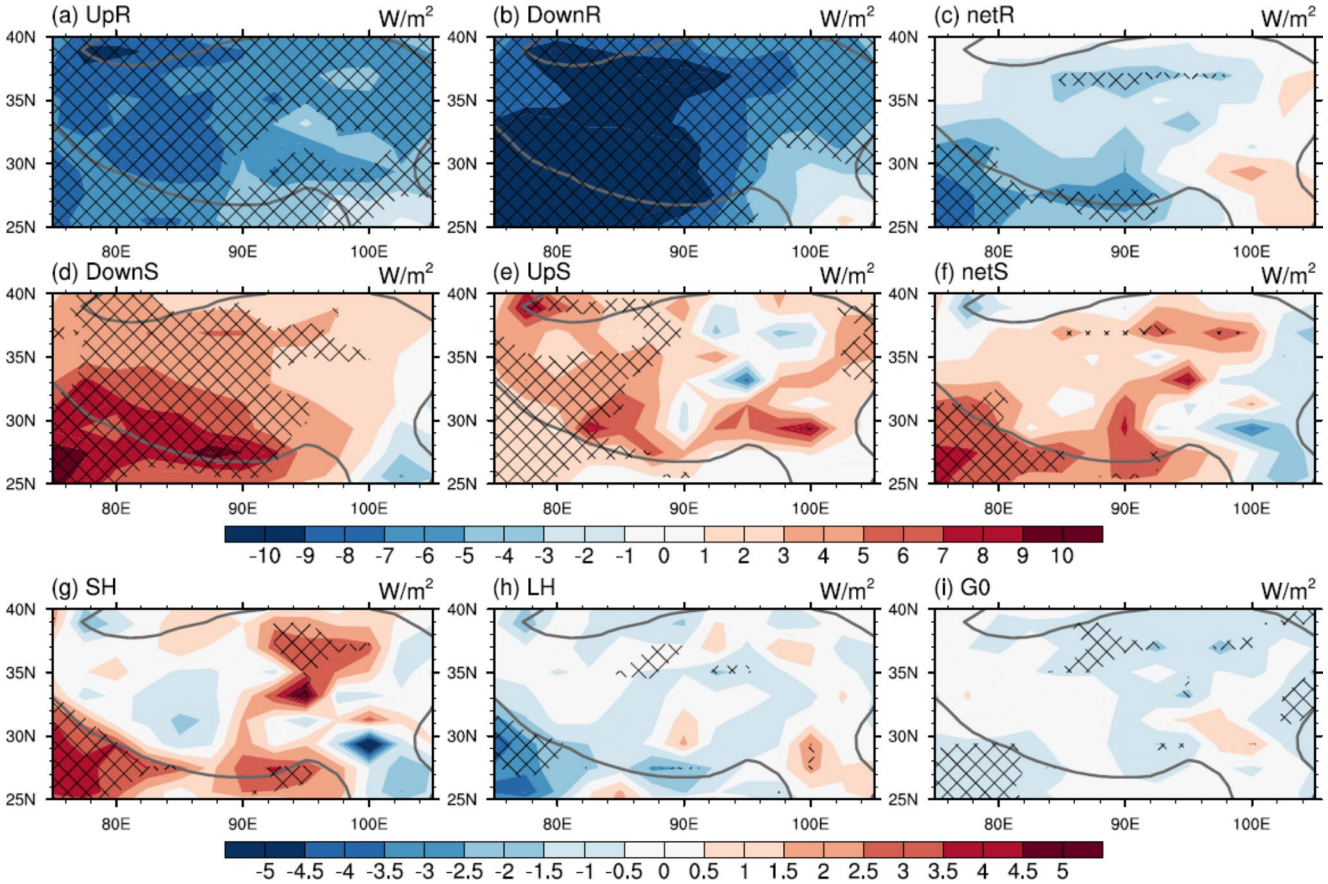

Fig. 6 Spatial patterns of difference, between CTRL and SEN-ALL, in DJF-mean surface **a** upwelling LW radiation, **b** downwelling LW radiation, **c** net LW radiation (positive value indicating downward radiation), **d** downwelling SW radiation, **e** upwelling SW radiation, **f** net SW radiation (positive value indicating downward radiation), **g** sensible heat flux, **h** latent heat flux, and **i** ground heat flux (units: W m^{-2}). The cross-slashed areas indicate the shaded values that exceed the 95% confidence level of statistical significance. The grey solid lines denote the topographic height of 1500 m

and Fig. 9b, c, and d illustrate the changes in 300-hPa heat flux divergence of SEN-ALL, SEN-PAC, and SEN-ALL6 with respect to CTRL. Under the forcing of tropical SST bias, heat flux exhibits an anomalous divergence over the main body of the plateau, with a small convergence area over the southeastern TP (Fig. 9b). The analogous pattern between Fig. 9a and b strongly suggests that the atmospheric dynamic processes related to heat transport are responsible for the atmospheric cooling leading to a decreased DLWRF and then a colder surface over the TP. Moreover, giving the obvious cold bias over the TP in all SEN-ALL, SEN-PAC, and SEN-ALL6 (Fig. 5m), the linkage between the tropical SST bias and the TP SAT in SEN-ALL may also exist in the other two cases. Figure 9c and d reveal an apparent heat flux divergence over the main body of the TP, which indicates that, when considering the forcing of the tropical SST bias over the Pacific Ocean or the tropical SST bias derived from the CMIP6 MME, there would be an analogous heat flux divergence over the TP, leading to a cooling atmosphere and then a reduced DLWRF and a colder surface over the TP. This linkage between tropical SST bias and TP SAT in experiment SEN-ALL is also applicable for experiments SEN-PAC and SEN-ALL6.

To further explore which component of the large-scale circulation is responsible for the energy divergence over the TP, 300-hPa heat flux and its divergence are analyzed. In Fig. 10a, b, and c, the vectors show the climatological mean heat flux of CTRL (the meridional component ($\bar{V} \bullet \bar{T}$) is doubled for a clearer view) and the shadings display the meridional component of heat flux divergence (i.e. $-\frac{\partial\left(\bar{V}\bullet\bar{T}\right)}{\partial y}$), the zonal component of heat flux divergence (i.e. $-\frac{\partial\left(\bar{U}\bullet\bar{T}\right)}{\partial x}$), and the sum of the two, respectively. For climatological mean, the meridional component is mainly convergent and the zonal component is divergent due to an accelerated jet stream over the TP and its east (Fig. 10a and b). The sum of the heat flux divergence shows a convergence over the eastern TP and a divergence over the western TP (Fig. 10c). Compared with CTRL, the heat flux change exhibits a cyclonic circulation over the western TP, accompanied by a stronger zonal heat transport along 30°N and a

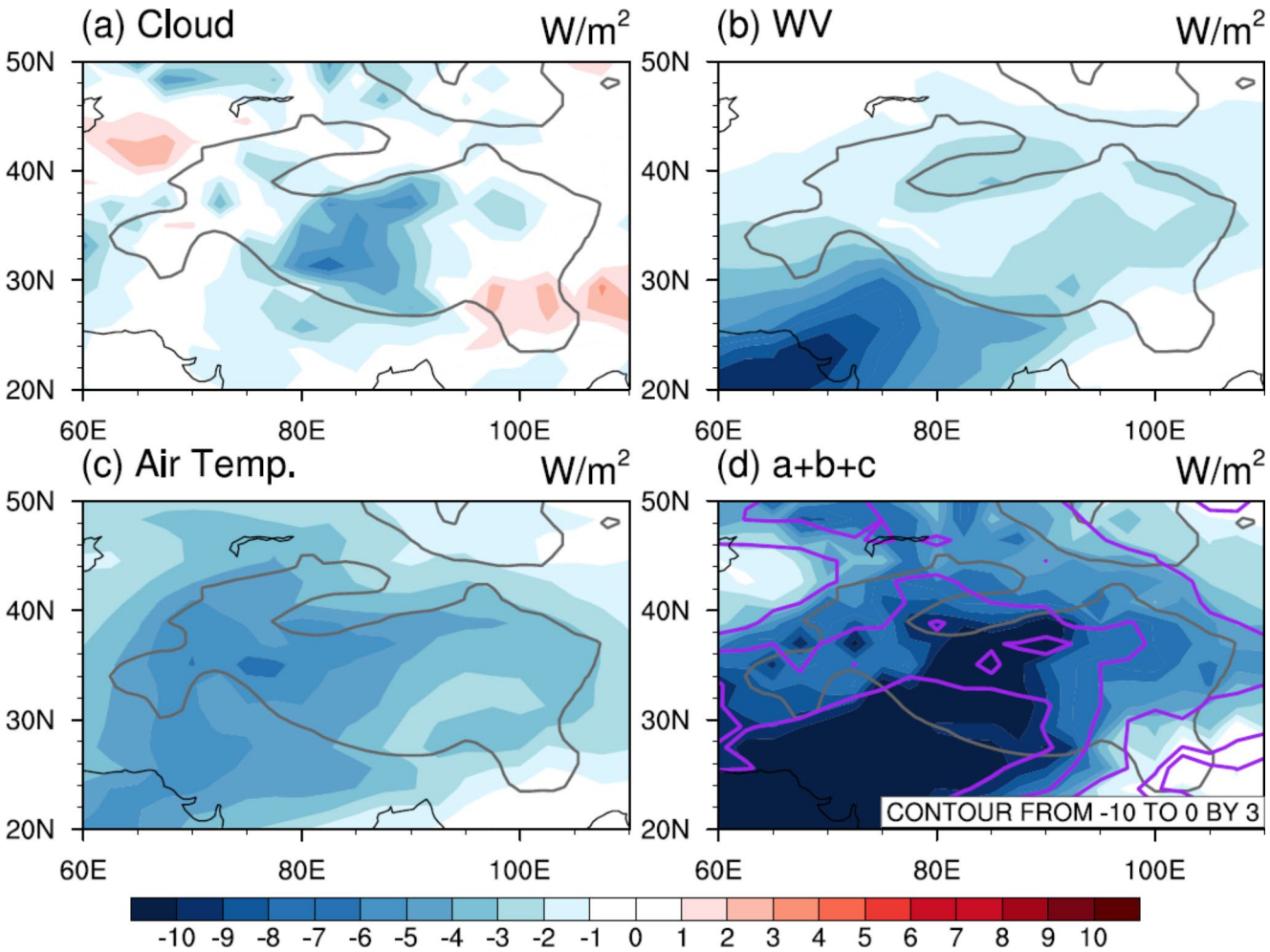

Fig. 7 Spatial pattern of partial perturbations of the surface downward LW radiative flux (units: W m^{-2}) in DJF-mean due to **a** cloud change alone, **b** water vapor change alone, **c** air temperature change alone, and **d** the shading denotes the sum of **a–c**, the contour denotes total perturbation of the surface DLWRF in SEN-ALL with respect to CTRL. Note that the cloud induced partial perturbation of downward LW radiative surface energy flux is corrected by using the pattern-amplitude projection method (see the text for details). The grey solid lines denote the topographic height of 1500 m

weaker poleward and equatorward heat transport over the southern TP and the northern TP, respectively (vectors in Fig. 10d, e, and f, for the difference between SEN-ALL and CTRL). Therefore, the change in the meridional component of heat flux divergence shows an apparent divergence over the TP along with its southern flank and a convergence over the western TP (Fig. 10d), while the change in the zonal component presents an anomalous convergence over the southeastern TP and a remarkable divergence over the western TP (Fig. 10e). Overall, the sum of the change in heat flux divergence (Fig. 10f) depicts an obvious energy divergence over the entire TP, except for a small energy convergence over the southeastern TP. Therefore, due to the forcing of tropical SST bias, the change in heat flux shows an anomalous divergence over the TP and the atmospheric cools down consequently, resulting in a decrease in DLWRF at the surface. The changes in heat flux at other levels present similar patterns with Fig. 10f, although the convergence and divergence areas move northward with increasing altitudes (Fig. S3 in the supplemental materials).

In short, our physical analysis provides a mechanical understanding of the link of TP cold bias to tropical SST biases. In response to the tropical SST biases, the westerly jet stream tends to intensify above the TP, which leads to more energy transported out of the plateau, causing a cold air bias above the TP. The cold air results in a reduction of downward thermal radiative energy fluxes at the surface, manifesting the TP cold bias.

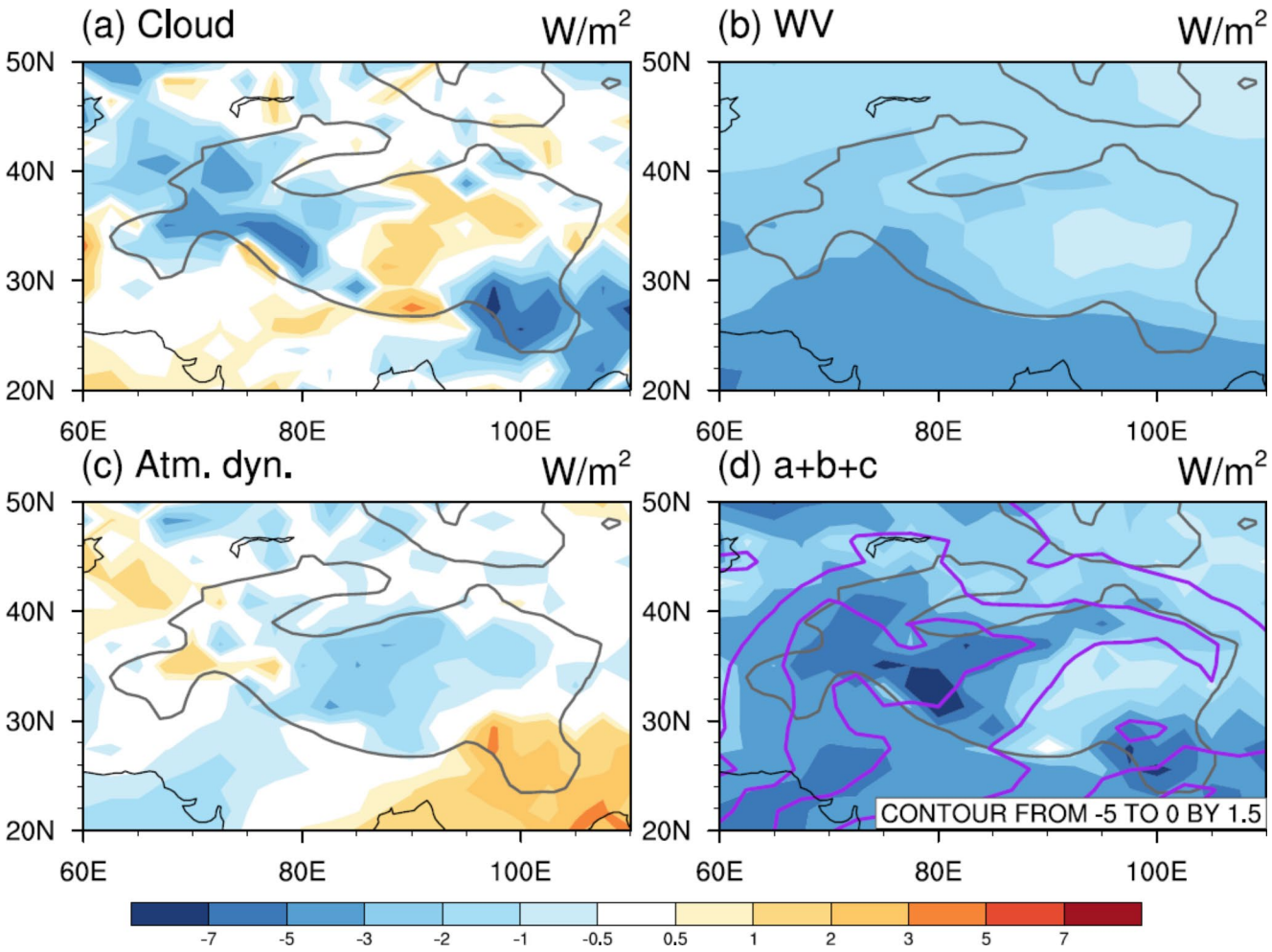

Fig. 8 Spatial pattern of partial surface downward LW radiative fluxes (units: W m^{-2}) in DJF-mean due to the partial air temperature changes whose thermal radiative cooling rates are in balance with **a** radiative heating rate perturbations induced by cloud change, **b** radiative heating rate perturbations induced by water vapor change, **c** nonradiative heating rate perturbations associated with atmospheric advective/convective processes, and **d** the shading denotes the sum of **a**–**c**, the contour denotes perturbation of the surface DLWRF due to air temperature change alone. Note that the atmospheric dynamic processes induced partial perturbation of DLWRF is corrected by using the pattern-amplitude projection method (see the text for details). The grey solid lines denote the topographic height of 1500 m

5 Conclusions

Compared with observational gridded data, the CMIP5 and CMIP6 models underestimate the SAT over the TP. While previous studies have been focused on local land surface factors such as the overestimation of surface albedo, in this study we explore the role of tropical SST bias as a critical remote external forcing in determining the characteristics of surface energy budget and its influence on the bias of the TP SAT. First, we display the systematic cold bias over the TP and the bias over the tropical oceans in both CMIP5 and CMIP6 models. The cold bias over the TP is larger in the cold season than in the warm season. Compared with the CMIP5, the CMIP6 MME shows an obvious improvement in reducing the bias in summer but with a comparable bias in winter. The systematic tropical SST bias exhibits a small annual cycle, with a negative bias over a large portion of the oceans and a small positive bias in the east coast of the mainland. The significant tropical SST bias largely overlaps the high correlation between the TP SAT and the tropical SST, indicating the potential impact of the SST bias on the TP SAT in the models.

A series of model experiments have been conducted to understand the influence of remote tropical SST bias forcing on the TP SAT. A surface energy budget analysis shows that, under the forcing of tropical SST bias, the DLWRF decreases significantly, and thus the surface gains less energy and a colder surface appears. The decomposition of the decreased DLWRF indicates that the cooling atmosphere over the TP is the main contributor and that the anomalous heat flux divergence induced mainly by weaker meridional heat flux convergence is responsible for the cooling of the

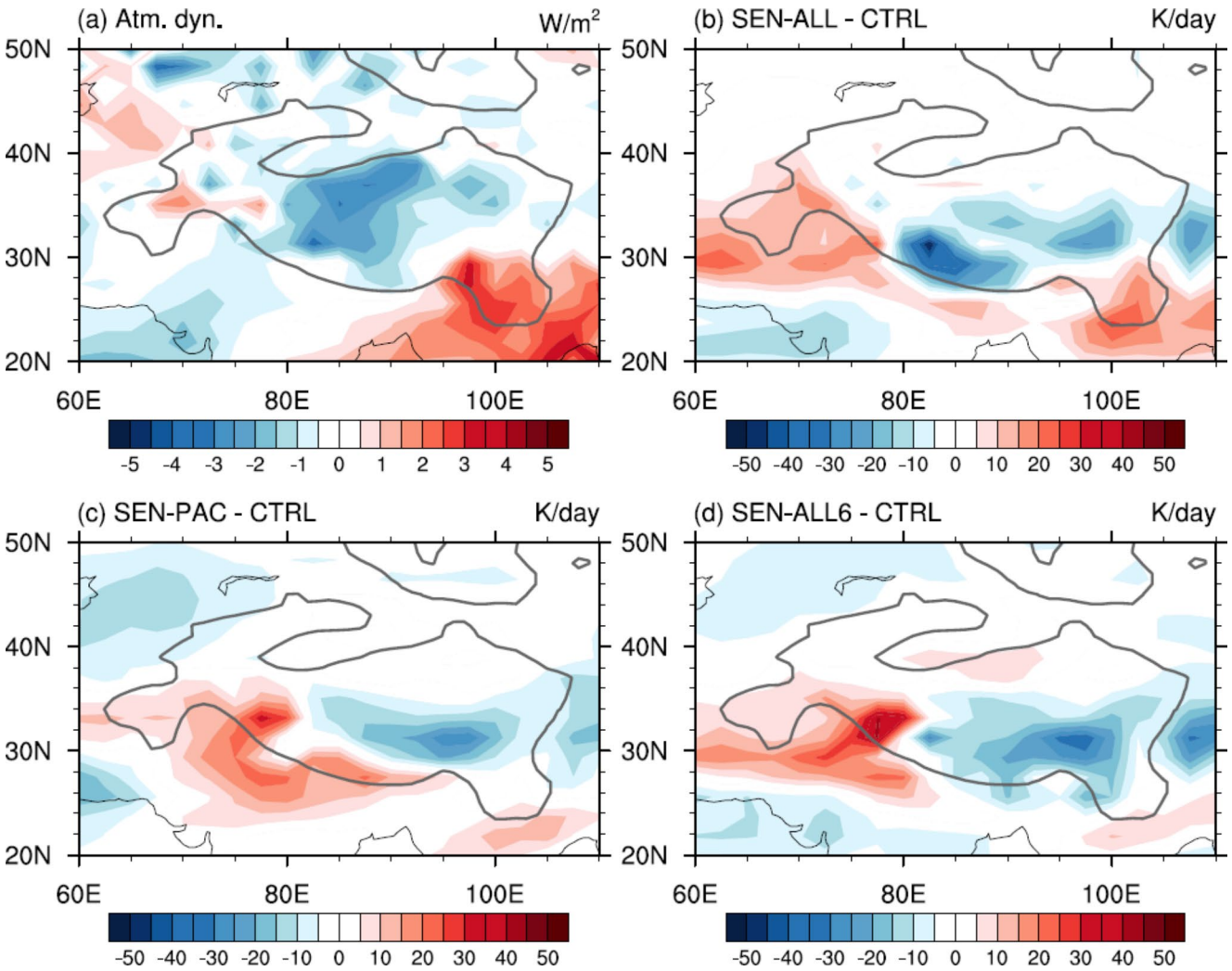

Fig. 9 **a** Spatial pattern of partial downward LW radiative surface energy fluxes (units: W m^{-2}) in DJF-mean due to the partial air temperature changes whose thermal radiative cooling rates are in balance with the nonradiative heating rate perturbations associated with atmospheric advective/convective processes, which is the same as in Fig. 8c with a different color bar. **b** Changes in DJF-mean horizontal heat flux divergence (units: K day^{-1}) at 300 hPa in SEN-ALL with respect to CTRL. **c** Changes in DJF-mean horizontal heat flux divergence (units: K day^{-1}) at 300 hPa in SEN-PAC with respect to CTRL. **d** Changes in DJF-mean horizontal heat flux divergence (units: K day^{-1}) at 300 hPa in SEN-ALL6 with respect to CTRL. The grey solid lines denote the topographic height of 1500 m

atmosphere. Importantly, the tropical Pacific SST bias forcing from the CMIP5 MME and the all-basin tropical SST bias forcing derived from the CMIP6 MME can both generate the linkage discussed above.

In short, climate models suffer from systematic tropical SST bias that influences heat transfer, leading to a cooled atmosphere and a reduced DLWRF and thus a colder surface over the TP. The tropical SST bias in the CMIP5 and CMIP6 models explains about 40% of the total cold bias over the TP.

It should be pointed out that although we have established a strong relationship between tropical SST and TP SAT and explained the response of TP SAT bias to the SST bias via a series of model experiments and diagnostic analyses, the physical process connecting the biases of SST and TP SAT has not been fully clarified. For example, how the tropical SST bias causes the change in the subtropical westerly jet stream needs to be better explained. One may also notice that there is a strong annual cycle of the TP SAT bias response to the tropical SST bias forcing which exhibits a neglectable annual cycle. The meridional migration of the climatological subtropical westerly jet stream may be responsible for the distinct TP responses between summer and winter. The climatological westerly jet stream is more or less located over the TP in winter but moves to the north of the TP in summer. The westerly anomalies above the TP in response to the tropical SST anomalies may exert a stronger impact in winter because they are directly superimposed on the westerly jet core. Furthermore, while the collective contributions of SST biases in all three tropical basins to

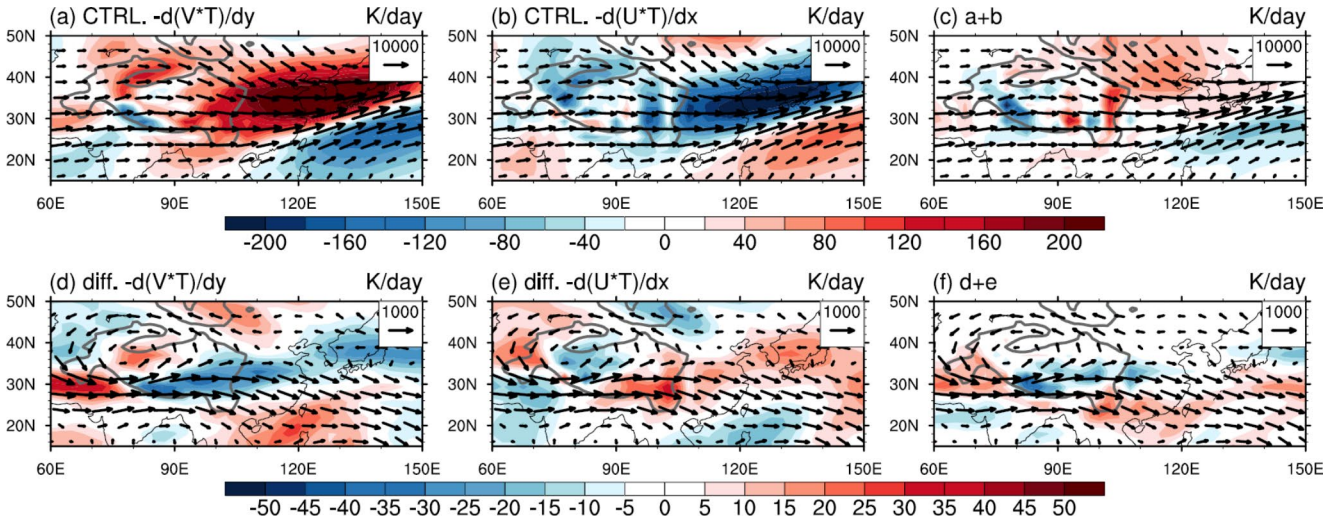

Fig. 10 Climatological DJF means of **a** meridional heat flux divergence (shading, units: K day^{-1}) and **b** zonal heat flux divergence (shading, units: K day^{-1}) at 300 hPa in CTRL. **c** presents the sum of horizontal heat flux divergence in **a** and **b**. Vectors in **a–c** indicate the climatological mean of heat flux (units: K m s^{-1}, the meridional component has been doubled) at 300 hPa in CTRL. Difference in DJF means of **d** meridional heat flux divergence (shading, units: K day^{-1}) and **e** zonal heat flux divergence (shading, units: K day^{-1}) at 300 hPa between CTRL and SEN-ALL. **f** presents the sum of horizontal heat flux divergence in **d** and **e**. The vectors in **d–f** indicate the difference in heat flux (units: K m s^{-1}, the meridional component has been doubled) at 300 hPa between CTRL and SEN-ALL. The grey solid lines denote the topographic height of 1500 m

the TP cold bias has been addressed in this study, the relative roles of the individual tropical ocean basins should be investigated in future studies.

Supplementary Information The online version contains supplementary material available at https://doi.org/10.1007/s00382-022-06421-y.

Acknowledgements We would thank Prof. Yi Deng of the Georgia Institute of Technology and Prof. Ziqian Wang of the Sun Yat-sen University for several helpful discussions. This study was jointly supported by the National Natural Science Foundation of China (Grants 42088101 and 42075028), the Guangdong Major Project of Basic and Applied Basic Research (Grant 2020B0301030004), the Guangdong Province Key Laboratory for Climate Change and Natural Disaster Studies (Grant 2020B1212060025), and the Jiangsu Collaborative Innovation Center for Climate Change.

Data Availability The monthly mean surface air temperature data from the National Meteorological Information Center, China Meteorological Administration, is available at http://data.cma.cn/data/cdcdetail/dataCode/SURF_CLI_CHN_TEM_MON_GRID_0.5.html. The monthly mean sea surface temperature from the ERSSTv5 dataset is available at https://www.ncdc.noaa.gov/data-access/marineocean-data/extended-reconstructed-sea-surface-temperature-ersst-v5. The CMIP5 and CMIP6 data are provided at https://esgf-node.llnl.gov/search/cmip5/ and https://esgf-node.llnl.gov/search/cmip6/, respectively.

References

Cai M, Lu J (2009) A new framework for isolating individual feedback processes in coupled general circulation climate models. Part II: Method demonstrations and comparisons. Clim Dyn 32:887–900. https://doi.org/10.1007/s00382-008-0424-4

Chen L, Frauenfeld OW (2014) Surface air temperature changes over the twentieth and twenty-first centuries in China simulated by 20 CMIP5 models. J Clim 27:3920–3937. https://doi.org/10.1175/JCLI-D-13-00465.1

Davey M, Huddleston M, Sperber K et al (2002) STOIC: A study of coupled model climatology and variability in tropical ocean regions. Clim Dyn 18:403–420. https://doi.org/10.1007/s00382-001-0188-6

de Szoeke SP, Fairall CW, Wolfe DE, Bariteau L, Zuidema P (2010) Surface flux observations on the southeastern tropical Pacific Ocean and attribution of SST errors in coupled ocean-atmosphere models. J Clim 23:4152–4174. https://doi.org/10.1175/2010JCLI3411.1

DeWitt DG (2005) Diagnosis of the tropical Atlantic near-equatorial SST bias in a directly coupled atmosphere-ocean general circulation model. Geophys Res Lett 32:1–4. https://doi.org/10.1029/2004GL021707

Duan A, Wu G (2005) Role of the Tibetan Plateau thermal forcing in the summer climate patterns over subtropical Asia. Clim Dyn 24:793–807. https://doi.org/10.1007/s00382-004-0488-8

Duan A, Xiao Z, Hu J (2014) Can current AGCMs reproduce historical changes in the atmospheric diabatic heating over the Tibetan Plateau? Atmos Ocean Sci Lett 7:143–148. https://doi.org/10.3878/j.issn.1674-2834.13.0084

Exarchou E, Prodhomme C, Brodeau L, Guemas V, Doblas-Reyes F (2018) Origin of the warm eastern tropical Atlantic SST bias in a climate model. Clim Dyn 51:1819–1840. https://doi.org/10.1007/s00382-017-3984-3

Flohn H (1957) Large-scale aspects of the "summer monsoon" in South and East Asia. J Meteorol Soc Japan Ser II 35A:180–186. https://doi.org/10.2151/jmsj1923.35A.0_180

Fu Q, Liou KN (1992) On the correlated k-distribution method for radiative transfer in nonhomogeneous atmosphere. J Atmos Sci 49:2193-2156. https://doi.org/10.1175/1520-0469(1992)049<2139:OTCDMF>2.0.CO;2

Fu Q, Liou KN (1993) Parameterization of the radiativer properties of cirrus clouds. J Atmos Sci 50:2008-2025. https://doi.org/10.1175/1520-0469(1993)050<2008:POTRPO>2.0.CO;2

Ghatak D, Sinsky E, Miller J (2014) Role of snow-albedo feedback in higher elevation warming over the Himalayas, Tibetan Plateau and Central Asia. Environ Res Lett 9:114008. https://doi.org/10.1088/1748-9326/9/11/114008

He B, Liu Y, Wu G, Wang Z, Bao Q (2019) The role of air–sea interactions in regulating the thermal effect of the Tibetan–Iranian Plateau on the Asian summer monsoon. Clim Dyn 52:4227–4245. https://doi.org/10.1007/s00382-018-4377-y

Hu Q, Jiang D, Fan G (2014) Evaluation of CMIP5 models over the Qinghai–Tibetan Plateau. Chin J Atmos Sci 38:924–938. https://doi.org/10.3878/j.issn.1006-9895.2013.13197(in Chinese)

Hu X, Li Y, Yang S, Deng Y, Cai M (2017) Process-based decomposition of the decadal climate difference between 2002-13 and 1984-95. J Clim 30:4373–4393. https://doi.org/10.1175/JCLI-D-15-0742.1

Huang B, Thorne PW, Banzon VF et al (2017) Extended reconstructed sea surface temperature, version 5 (ERSSTv5): Upgrades, validations, and intercomparisons. J Clim 30:8179–8205. https://doi.org/10.1175/JCLI-D-16-0836.1

Hurrell JW, Hack JJ, Shea D, Caron JM, Rosinski J (2008) A new sea surface temperature and sea ice boundary dataset for the community atmosphere model. J Clim 21:5145–5153. https://doi.org/10.1175/2008JCLI2292.1

Hurrell JW, Holland MM, Gent PR et al (2013) The community earth system model: A framework for collaborative research. Bull Am Meteorol Soc 94:1339–1360. https://doi.org/10.1175/BAMS-D-12-00121.1

Ji C, Zhang Y, Cheng Q, Li Y, Jiang T, Liang X (2018) On the relationship between the early spring Indian Ocean's sea surface temperature (SST) and the Tibetan Plateau atmospheric heat source in summer. Glob Planet Change 164:1–10. https://doi.org/10.1016/j.gloplacha.2018.02.011

Jia K, Ruan Y, Yang Y, You Z (2019) Assessment of CMIP5 GCM simulation performance for temperature projection in the Tibetan Plateau. Earth Space Sci 6:2362–2378. https://doi.org/10.1029/2019EA000962

Kang H, Choi YS, Hwang J, Kim HS (2020) On the cloud radiative effect for tropical high clouds overlying low clouds. Geosci Lett 7. https://doi.org/10.1186/s40562-020-00156-6

Kurian J, Li P, Chang P, Patricola CM, Small J (2021) Impact of the Benguela coastal low-level jet on the southeast tropical Atlantic SST bias in a regional ocean model. Clim Dyn 56:2773–2800. https://doi.org/10.1007/s00382-020-05616-5

Lee WL, Li JLF, Xu KM et al (2019) Relating precipitating ice radiative effects to surface energy balance and temperature biases over the Tibetan Plateau in winter. J Geophys Res Atmos 124:12455–12467. https://doi.org/10.1029/2018JD030204

Li G, Xie SP (2012) Origins of tropical-wide SST biases in CMIP multi-model ensembles. Geophys Res Lett 39. https://doi.org/10.1029/2012GL053777

Li G, Xie SP (2014) Tropical biases in CMIP5 multimodel ensemble: The excessive equatorial Pacific cold tongue and double ITCZ problems. J Clim 27:1765–1780. https://doi.org/10.1175/JCLI-D-13-00337.1

Lu J, Cai M (2009) Seasonality of polar surface warming amplification in climate simulations. Geophys Res Lett 36:L16704. https://doi.org/10.1029/2009GL040133

Lu M, Yang S, Li Z, He B, He S, Wang Z (2018) Possible effect of the Tibetan Plateau on the "upstream" climate over West Asia, North Africa, South Europe and the North Atlantic. Clim Dyn 51:1485–1498. https://doi.org/10.1007/s00382-017-3966-5

Lu M, Huang B, Li Z, Yang S, Wang Z (2019) Role of Atlantic air-sea interaction in modulating the effect of Tibetan Plateau heating on the upstream climate over Afro-Eurasia-Atlantic regions. Clim Dyn 53:509–519. https://doi.org/10.1007/s00382-018-4595-3

Lun Y, Liu L, Cheng L et al (2021) Assessment of GCMs simulation performance for precipitation and temperature from CMIP5 to CMIP6 over the Tibetan Plateau. Int J Climatol 41:3994–4018. https://doi.org/10.1002/joc.7055

Ma J, Guan X, Guo R, Gan Z, Xie Y (2017) Mechanism of non-appearance of hiatus in Tibetan Plateau. Sci Rep 7:4421. https://doi.org/10.1038/s41598-017-04615-7

Mechoso CR, Robertson AW, Barth N, et al (1995) The seasonal cycle over the tropical Pacific in coupled ocean-atmosphere general circulation models. Mon Wea Rev 123:2825-2838. https://doi.org/10.1175/1520-0493(1995)123<2825:TSCOTT>2.0.CO;2

Meng X, Lyu S, Zhang T et al (2018) Simulated cold bias being improved by using MODIS time-varying albedo in the Tibetan Plateau in WRF model. Environ Res Lett 13:044028. https://doi.org/10.1088/1748-9326/aab44a

Neale RB, Richter J, Park S et al (2013) The mean climate of the community atmosphere model (CAM4) in forced SST and fully coupled experiments. J Clim 26:5150–5168. https://doi.org/10.1175/JCLI-D-12-00236.1

Peng Y, Duan A, Hu W et al (2022) Observational constraint on the future projection of temperature in winter over the Tibetan Plateau in CMIP6 models. Enviro Res Lett. https://doi.org/10.1088/1748-9326/AC5371

Rangwala I, Miller JR, Russell GL, Xu M (2010) Using a global climate model to evaluate the influences of water vapor, snow cover and atmospheric aerosol on warming in the Tibetan Plateau during the twenty-first century. Clim Dyn 34:859–872. https://doi.org/10.1007/s00382-009-0564-1

Rapizo H, Babanin AV, Schulz E, Hemer MA, Durrant TH (2015) Observation of wind-waves from a moored buoy in the Southern Ocean. Ocean Dyn 65:1275–1288. https://doi.org/10.1007/s10236-015-0873-3

Russell JL, Kamenkovich I, Bitz C et al (2018) Metrics for the evaluation of the Southern Ocean in coupled climate models and earth system models. J Geophys Res Ocean 123:3120–3143. https://doi.org/10.1002/2017JC013461

Sejas SA, Cai M (2016) Isolating the temperature feedback loop and its effects on surface temperature. J Atmos Sci 73:3287–3303. https://doi.org/10.1175/JAS-D-15-0287.1

Shaman J, Tziperman E (2005) The effect of ENSO on Tibetan Plateau snow depth: A stationary wave teleconnection mechanism and implications for the south Asian monsoons. J Clim 18:2067–2079. https://doi.org/10.1175/JCLI3391.1

Song Z, Qiao F, Song Y (2012) Response of the equatorial basin-wide SST to non-breaking surface wave-induced mixing in a climate model: An amendment to tropical bias. J Geophys Res Ocean 117. https://doi.org/10.1029/2012JC007931

Su F, Duan X, Chen D, Hao Z, Cuo L (2013) Evaluation of the global climate models in the CMIP5 over the Tibetan Plateau. J Clim 26:3187–3208. https://doi.org/10.1175/JCLI-D-12-00321.1

Sumner MD, Michael KJ, Bradshaw CJA, Hindell MA (2003) Remote sensing of Southern Ocean sea surface temperature: Implications

for marine biophysical models. Remote Sens Environ 84:161–173. https://doi.org/10.1016/S0034-4257(02)00103-7

Wang B, Bao Q, Hoskins B, Wu G, Liu Y (2008) Tibetan Plateau warming and precipitation changes in East Asia. Geophys Res Lett 35:L14702. https://doi.org/10.1029/2008GL034330

Wang C, Yu L, Huang B (2012) The impact of warm pool SST and general circulation on increased temperature over the Tibetan Plateau. Adv Atmos Sci 29:274–284. https://doi.org/10.1007/s00376-011-1034-3

Wang S, Zhang M, Sun M et al (2015) Comparison of surface air temperature derived from NCEP/DOE R2, ERA-Interim, and observations in the arid northwestern China: a consideration of altitude errors. Theor Appl Climatol 119:99–111. https://doi.org/10.1007/s00704-014-1107-1

Wang Y, Xu X (2018) Impact of ENSO on the thermal condition over the Tibetan Plateau. J Meteorol Soc Japan 96:269–281. https://doi.org/10.2151/jmsj.2018-032

Wang Z, Duan A, Yang S (2019) Potential regulation on the climatic effect of Tibetan Plateau heating by tropical air–sea coupling in regional models. Clim Dyn 52:1685–1694. https://doi.org/10.1007/s00382-018-4218-z

Xie SP, Miyama T, Wang Y et al (2007) A regional ocean–atmosphere model for Eastern Pacific climate: Toward reducing tropical biases. J Clim 20:1504–1522. https://doi.org/10.1175/JCLI4080.1

Xie Z, Wang B (2021) Summer heat sources changes over the Tibetan Plateau in CMIP6 models. Environ Res Lett 16:064060. https://doi.org/10.1088/1748-9326/ac0279

Xu Z, Chang P, Richter I, Kim W, Tang G (2014) Diagnosing southeast tropical Atlantic SST and ocean circulation biases in the CMIP5 ensemble. Clim Dyn 43:3123–3145. https://doi.org/10.1007/s00382-014-2247-9

Xue Y, Diallo I, Li W et al (2018) Spring land surface and subsurface temperature anomalies and subsequent downstream late spring-summer droughts/floods in North America and East Asia. J Geophys Res Atmos 123:5001–5019. https://doi.org/10.1029/2017JD028246

Yanai M, Li C, Song Z (1992) Seasonal heating of the Tibetan Plateau and its effects on the evolution of the Asian summer monsoon. J Meteorol Soc Japan Ser II 70:319–351. https://doi.org/10.2151/jmsj1965.70.1B_319

Yang K, Rasmy M, Rauniyar S et al (2007) Initial CEOP-based review of the prediction skill of operational general circulation models and land surface models. J Meteorol Soc Japan 85A:99–116. https://doi.org/10.2151/jmsj.85A.99

You Q, Min J, Kang S (2016) Rapid warming in the Tibetan Plateau from observations and CMIP5 models in recent decades. Int J Climatol 36:2660–2670. https://doi.org/10.1002/joc.4520

Yu H, Luedeling E, Xu J (2010) Winter and spring warming result in delayed spring phenology on the Tibetan Plateau. Proc Natl Acad Sci 107:22151–22156. https://doi.org/10.1073/pnas.1012490107

Zhang L, Wang C, Song Z, Lee SK (2014) Remote effect of the model cold bias in the tropical North Atlantic on the warm bias in the tropical southeastern Pacific. J Adv Model Earth Syst 6:1016–1026. https://doi.org/10.1002/2014MS000338

Zhang P, Gao L, Mao X (2006) Primary analyses of teleconnection relationship between the Qinghai Xizang Plateau air temperature and the Indian Ocean SST. Plateau Meteorol 25:800–806. (in Chinese)

Zhao T, Guo W, Fu C (2008) Calibrating and evaluating reanalysis surface temperature error by topographic correction. J Clim 21:1440–1446. https://doi.org/10.1175/2007JCLI1463.1

Zhao Y, Duan A, Wu G (2018) Interannual variability of late-spring circulation and diabatic heating over the Tibetan Plateau associated with Indian Ocean forcing. Adv Atmos Sci 35:927–941. https://doi.org/10.1007/s00376-018-7217-4

Zhou S, Huang G, Huang P (2020) Excessive ITCZ but negative SST biases in the tropical Pacific simulated by CMIP5/6 models: The role of the meridional pattern of SST bias. J Clim 33:5305–5316. https://doi.org/10.1175/JCLI-D-19-0922.1

Zhuo H, Liu Y, Jin J (2016) Improvement of land surface temperature simulation over the Tibetan Plateau and the associated impact on circulation in East Asia. Atmos Sci Lett 17:162–168. https://doi.org/10.1002/asl.638